Reports on Progress in **Physics**

PURPOSE-LED PUBLISHING™

LETTER • **OPEN ACCESS**

Nucleation kinetics and virtual melting in shear-induced structural transitions

To cite this article: Wei Li *et al* 2025 *Rep. Prog. Phys.* **88** 010501

OPEN ACCESS
IOP Publishing

Letters
Reports on Progress in Physics

Rep. Prog. Phys. **88** (2025) 010501 (7pp)
https://doi.org/10.1088/1361-6633/ad99fd

Letter

Nucleation kinetics and virtual melting in shear-induced structural transitions

Wei Li[1], Yi Peng[2,3], Tim Still[4], A G Yodh[4] and Yilong Han[1,*]

[1] Department of Physics, Hong Kong University of Science and Technology, Clear Water Bay, Hong Kong Special Administrative Region of China, People's Republic of China
[2] Beijing National Laboratory for Condensed Matter Physics, Institute of Physics, Chinese Academy of Sciences, Beijing 100190, People's Republic of China
[3] School of Physical Sciences, University of Chinese Academy of Sciences, Beijing 100049, People's Republic of China
[4] Department of Physics and Astronomy, University of Pennsylvania, Philadelphia, PA 19104, United States of America

E-mail: yilong@ust.hk

Received 6 August 2024, revised 9 November 2024
Accepted for publication 3 December 2024
Published 10 December 2024

Corresponding editor: Dr Paul Mabey

Abstract

Large shear deformations can induce structural changes within crystals, yet the microscopic kinetics underlying these transformations are difficult for experimental observation and theoretical understanding. Here, we drive shear-induced structural transitions from square (□) lattices to triangular (△) lattices in thin-film colloidal crystals and directly observe the accompanying kinetics with single-particle resolution inside the bulk crystal. When the oscillatory shear strain amplitude $0.1 \leqslant \gamma_m < 0.4$, △-lattice nuclei are surrounded by a liquid layer throughout their growth due to localized shear strain at the interface. Such virtual melting at crystalline interface has been predicted in theory and simulation, but have not been observed in experiment. The mean liquid layer thickness is proportional to the shear which can be explained by the Lindemann melting criterion. This provides an alternative explanation on virtual melting.

Supplementary material for this article is available online

Keywords: crystal–crystal transition, shear-induced transition, nucleation kinetics, virtual melting, colloid

* Author to whom any correspondence should be addressed.

1. Introduction

Structural transitions between two polymorphic crystals, such as crystal–crystal (c–c) transitions, occur widely in metallurgy, ceramics, and even the earth's mantle, and they influence a broad range of applications in steel production and functional materials processing [1]. Compared to simpler transitions such as melting and crystallization, these transitions lack a group–subgroup relation between the symmetries of parent and product phases, which leads to transition kinetics with metastable intermediate structures that pose challenges for theory [2]. Subtle complexities arise from various types of defects and stresses produced during the transition. Unfortunately, since traditional x-ray diffraction and electron microscopy cannot routinely follow *in-situ* microscopic kinetics in bulk solids at the atomic level, the kinetic pathway mechanisms associated with structural changes remain poorly understood and difficult to predict.

In practice, many structural transitions are driven by mechanical deformation, e.g. olivine-spinel transformations in mantle [2] and during fabrication of metals [1] and super alloys [3]. As noted above, elucidation of such transitions, driven by athermal anisotropic forces, are challenging for theory and *in-situ* experiment. Thus, they have mainly been studied by simulation [4–11] and via measurements of post-mortem microstructures after unloading the strain [3]. The present contribution addresses these limitations, employing colloidal crystals composed of micron-size particles; the crystals are readily deformed to drive structural transitions, permitting *in-situ* observation of bulk kinetics with single-particle resolution [12].

Micron-sized colloidal particles can be viewed as 'big atom' because they have thermal Brownian motions and can form various phases at thermal equilibrium [12–14]. Colloids are outstanding model systems for phase transition studies because colloidal particles can be imaged directly by optical microscopy and their thermal motions can be tracked by image processing [15]. The simplest model of colloids is the hard-sphere system which free energy $F = U - TS = -TS$ because the interaction potential energy U is zero. T is temperature. Entropy S is mainly from the free-volume entropy which depends on the volume fraction ϕ, i.e. the ratio of the volume of all spheres to the total volume of the sample [12, 13]. In contrast to atomic systems dominated by atomic interaction energy, hard-sphere-like colloids are dominated by entropy and their phase behaviours are dictated by ϕ [13, 16]. $1/\phi$ in colloids plays a role of effective temperature in atomic systems [13]. Colloid experiments have provided important insights about structural transitions brought about by variation of volume fraction [17, 18] and particle interaction [19–25], and by application of electric fields to stretch the lattice [26, 27]. To date, various features of colloidal crystals in shear have been studied, including self-assembly [28, 29], grain coarsening and reorientation [30–34], grain boundary roughening [35], shear buckling [36] and banding [37], melting and crystallization [38–40], crystal–crystal transition [41]. However, the microscopic kinetics of shear-induced crystal–crystal transitions remain unexplored in experiment. Shear not only enhances particles' motions (i.e. effective temperature) but also drives the system out of equilibrium. Such nonequilibrium phase transitions are poorly understood. Here we observe distinct kinetics in different shear conditions; moreover, observations of nuclei growth provide first experimental evidence for strain-induced virtual melting (i.e. melting below melting point) [42], predicted in theory.

2. Methods

The colloidal crystals are composed of poly(N-isopropylacrylamide) (NIPA) microgel spheres in aqueous suspensions. They are thermal-sensitive with short-range repulsions, whose phase behavior is very similar to that of hard spheres [43]. The directly measured diameter of NIPA microgel spheres from imaging has a small ambiguity due to the diffraction and softness of the sphere. Therefore, the measured diameter $\sigma'(T)$ is slightly linearly rescaled to an effective diameter, $\sigma(T)$, so that the melting $\phi_m = 0.545$ is the same as those of the 3D hard spheres. Then, the freezing $\phi_f = 0.49$ is very close to 0.494 for hard spheres. [16, 44]. As a result, $\sigma(T)$, changes linearly from 1.04 μm at 25 °C to 0.89 μm at 30 °C (supplementary section 1). Our samples of NIPA spheres are confined between two walls at high volume fraction. They self-assemble into a cascade of crystalline phases as the effective wall separation H/σ increases [45–47]: monolayer triangular (1△); bilayer square (2□); 2△; … n□; n△ lattices ($n < 6$). Such phase behavior has been observed in colloids [17, 18, 48] and has been quantified in the phase diagram for hard spheres by simulation [45–47] (supplementary figure S2(c)). These crystals have distinct densities, thus transitions between them are expected to be first-order. By decreasing the volume fraction ϕ, we can induce the $n\square \rightarrow (n-1)\triangle$ transition.

In our experiments, a circular area ($\pi(60\ \mu m)^2$, approximately 1.2×10^4 particles) in the interior of a large single crystal domain of □ lattice is uniformly heated to be above the $\square \rightarrow \triangle$ transition volume fraction ϕ_c (≈ 0.58 at the corresponding $T_c = 28.0 \pm 0.1$ °C) and the ambient unheated area is below it. Thus, application of oscillatory shear can drive the homogeneous $\square \rightarrow \triangle$ transition, but only in the heated area. Here both the heating-induced volume-fraction decrease and the shear-induced effective temperature increase facilitate the transition.

A syringe pump is used to apply an oscillatory shear to the colloidal crystal. It produces a Couette-like velocity profile in the z direction (supplementary figures S1(b) and (c)). In such thin-film crystals, all the defect structures, including dislocations and interfaces, are the same for each layer. Thus, it is a quasi-2D sample and the middle layer is typically observed. In the interior of each crystal domain, the sliding velocity is also uniform in the xy plane. The measured shear strain γ oscillates with an amplitude γ_m and a period of 2.4 s. Particles are tracked by standard image analysis [15]. More experimental details are in supplementary information section 1.

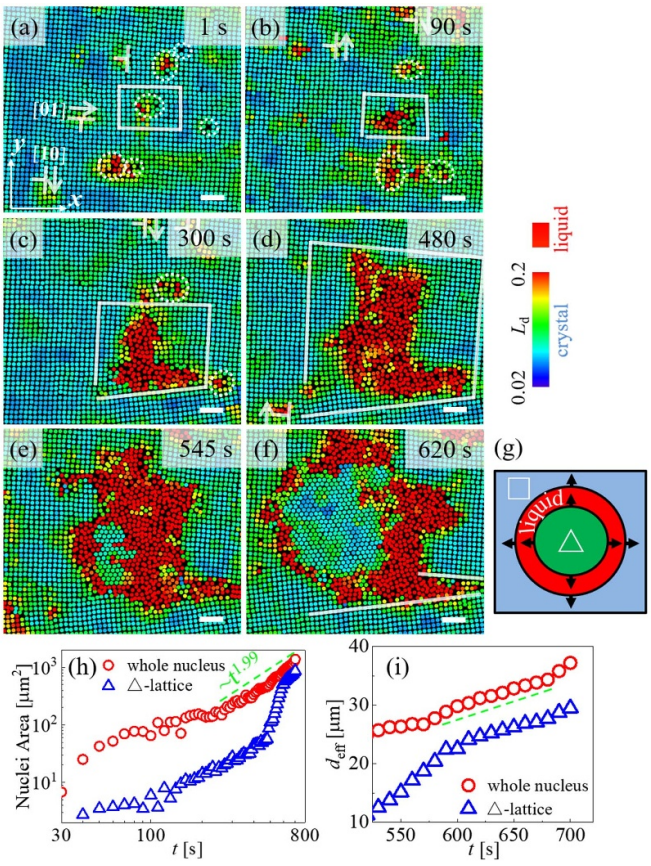

Figure 1. Nucleation of □ → △ transition under $\gamma_m = 0.3$ (movie S3). Color bar for (a)–(d): dynamic Lindemann parameter L_d (see supplementary information section 2.3). Scale bars: 5 μm. (a) Dislocations (⊥) glide (white arrows) along the [01] or [10] direction toward the pre-existing vacancy regions (dashed circles). Shear direction is along the x axis. (b) A [10] dislocation combines with a vacancy, resulting in a small liquid in the white Burgers loop. (c), (d) The liquid nucleus grows and absorbs more dislocations. (e), (f) A △ lattice nucleates from the liquid and surrounded by a liquid layer. The lattice distortion is indicated by white lines. (g) A schematic of a growing △-lattice nucleus covered with a liquid layer. (h) Size evolution of the whole nucleus (liquid + △ lattice) and its △-lattice part. (i) The effective nucleus diameters $d_{eff} = \sqrt{\text{nucleus area}}$ for the whole nucleus and for the △-lattice part are linear, with t with the same slope (dashed line) at $t > 600$ s.

3. Results

When $\gamma_m \leqslant 0.1$, the □ crystal directly transforms to the △ crystal via a martensitic nucleation (supplementary figures S7(a)–(d)). Under ultra-large shear strain with $\gamma_m \geqslant 0.4$, the crystals become unstable and melt directly.

3.1. Nuclei surrounded by virtual melt under $0.1 < \gamma_m < 0.4$

In the intermediate range of $0.1 < \gamma_m < 0.4$, the applied shear stress readily generates defects, such as dislocations and vacancies, and enhances their mobility (figure 1(a)) [1]. The rapid coalescence of these defects triggers the nucleation of a liquid phase; such a nucleus is shown with an unclosed Burgers loop in figures 1(a) and (b). The nucleus grows and absorbs more dislocations, which further opens the Burgers loop (figures 1(b)–(d)). This effect is similar to dislocation accumulation observed in a shear-induced crystal-to-amorphous transition in NiTi alloys [3] and silicon [49], but it is rarely observed in the nucleation process during c–c transitions. In the present case, the disordered region is a liquid rather than an amorphous solid, because particles actively swap positions (movies S3, S4). Later, when the liquid nucleus grows large, a small △ lattice nucleates within the liquid drop.

The nucleation process exhibits four stages: (1) For $t < 200$ s, the liquid nucleus is subcritical in size; (2) For $200\,\text{s} < t < 525$ s, a supercritical liquid nucleus is present with subcritical △-lattice nuclei inside it. Most subcritical △-lattice nuclei vanish and eventually one grows large; (3) For $525\,\text{s} < t < 600$ s, the △-lattice nucleus has passed its critical size and rapidly grows drawing particles from the liquid; (4) For $t > 600$ s, the △-lattice nucleus growth slows, and its speed is essentially the same as that of the liquid-□ interface. This complicated growth with multiple phases cannot be fit by a simple model in the early stages. However, in stage (4), the area of the whole nucleus grows at a rate $\propto t^2$ (figure 1(h)); alternatively, the effective nucleus diameter, $d_{eff} \propto t$ (figure 1(i)). This behavior corresponds to interface-reaction-limited growth described by Wilson–Frenkel law [1]: nucleus growth is determined by the constant particle incorporation rate from the parent phase to the nucleus, and thus the nucleus growth rate is proportional to nucleus perimeter and diameter d_{eff}.

Afterwards, for $t > 600$ s, the d_{eff} of liquid and △-lattice nuclei increase at the same rate (figure 1(i)); as a result, a liquid layer with a constant mean thickness is essentially sandwiched between the □ and △ lattices. Note however, while the mean thickness is approximately constant, the local thickness of the liquid ring strongly fluctuates for $600\,\text{s} < t < 1000$ s. These fluctuations are likely due to nuclei coalescence, which significantly redistributes the lattice strain (supplementary figure S8). A liquid ring with a more uniform thickness is observed during the latest stage, $t > 1000$ s, wherein the size of the △ lattice is much larger than mean liquid layer thickness (figure 2(a) and movie S4). In this situation, the liquid ring can reduce the interfacial strain energy. The interfacial strain arises near the □-△ interface but is absent near the liquid [42]. In practice, strains often localize at crystalline interfaces or grain boundaries [50]. Interestingly, under sufficiently strong shear conditions, the strain energy can be large enough such that the □-△ interface melts to form a liquid. The local thickness of the liquid layer is a constant for the interfaces along the shear and fluctuates strongly for the interfaces perpendicular to the shear direction because such interfaces tend to undergo a kinetic roughening process [35]. Nevertheless, the mean thickness of the liquid is a constant (figure 1(i)). Since the bulk equilibrium phase (with lowest chemical potential) is the △ crystal, this liquid layer is an interfacial wetting layer [51, 52] that

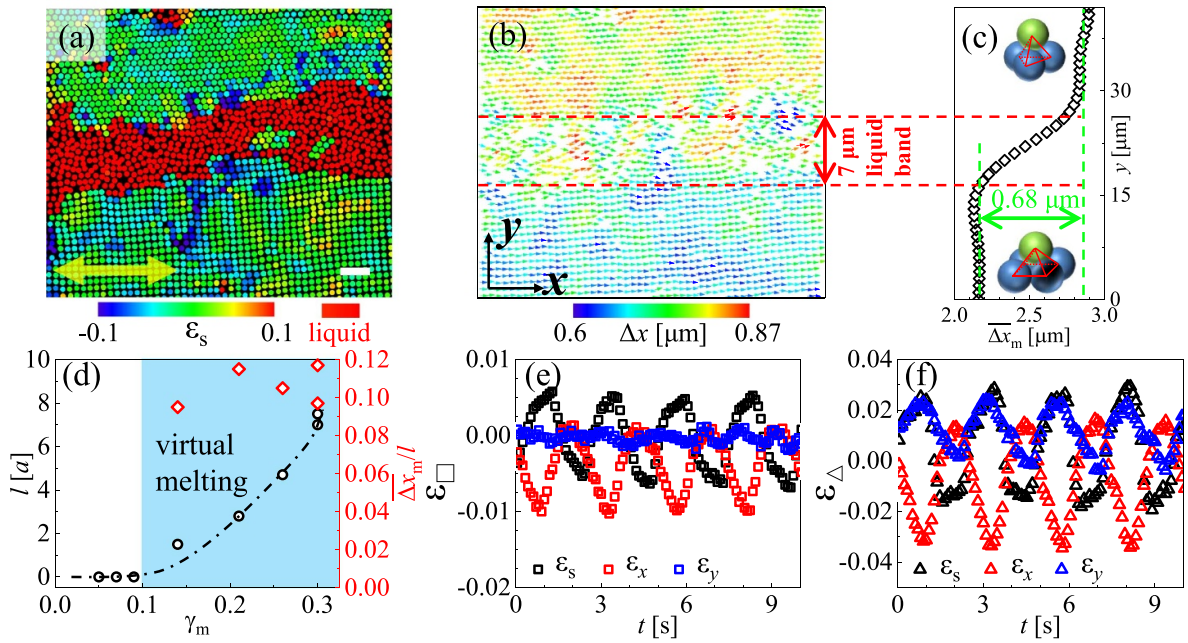

Figure 2. Shear-induced interfacial virtual melting. (a) Growth front of the nucleus in figure 1 at $t = 1300$ s. Particles are colored by ε_s. Scale bar: 5 μm. (b) Displacement vectors during 0.2 s for particles in (a). The images of a small fraction of liquid particles are blurry and thus their displacements are not tracked. (c) Distribution profile of the maximum displacement $\overline{\Delta x}_m$. Insets: The local packing structure of regular tetrahedron for the $\triangle$ lattice and square pyramid for the $\square$ lattice. (d) The mean liquid layer thickness l (circles) increases with γ_m. The shear displacement gradient (diamonds) $\overline{\Delta x}_m/l \sim 0.11 \pm 0.01$ under different γ_m. (e), (f) Mean local strain tensor components for the $\square$ and $\triangle$ lattices, respectively.

arises before the melting point is reached. This liquid-layer formation phenomenon is often called virtual melting [42]; it is reminiscent of premelting [51] but is not an equilibrium phenomenon.

The preexisting interface has an interfacial energy which reduces the free energy barrier of melting. Thus, melting tends to occur from interfaces [53, 54]. This mechanism can also result in interfacial premelting below melting temperature [43, 51, 52]. This interfacial energy under no shear should be much smaller than the interfacial strain energy under an external shear. The shear-induced strain energy vanishes after the formation of a liquid layer on the interface [8, 9]. Thus, the interface melts when [5]

$$\Gamma_{\triangle\text{-liquid}} + \Gamma_{\text{liquid-}\square} + \Delta G_{\square\text{-liquid}} < \Gamma_{\triangle\text{-}\square} + e_s, \qquad (1)$$

where Γ is the interfacial energy, $\Delta G_{\square\text{-liquid}}$ is the free energy difference between $\square$ lattice and liquid, and e_s is the strain energy due to external shear. The above inequality can hold under sufficiently large shear, i.e. a large enough e_s. Therefore, the interfacial energy is minimized by forming a $\triangle$-liquid interface and a liquid-$\square$ interface (e_s vanishes in liquid). However, Inequality (1) is based on free energies which are not rigorously defined under a non-equilibrium shear. Consequently, we provide an alternative mechanism in the next section.

3.2. *Mechanism of interfacial virtual melting*

In the latest stage, the $\square$ and $\triangle$ lattices slide with respect to one another with different amplitudes (figure 2(b)). The particle displacements along the shear direction, Δx, give rise to a displacement gradient across the liquid layer (figure 2(b)). $\Delta x(t)$ is oscillatory (supplementary figure S3(d)) as expected. The gradient of $\overline{\Delta x}_m$ across the 7 μm liquid layer is $0.68/7 \simeq 0.1$ (figure 2(c)). $\overline{\Delta x}_m/l$ is robust under different γ_m (figure 2(d)). Its value of 0.1 coincides with the Lindemann melting criterion. The Lindemann melting criterion states that a crystal begins to melt when L_d reaches a threshold value: melting from free surface when L_d reaches 0.1 and from bulk when L_d reaches 0.18 for many crystals [54, 55]. The Lindemann melting criterion has been demonstrated to hold well in equilibrium and non-equilibrium steady states [39, 43, 56]. L_d is the ratio of the particle mean displacement amplitude to the lattice constant. $\overline{\Delta x}_m/l$ can be viewed as the shear-induced displacement on each particle relative to a lattice constant (supplementary figures S4(b) and (c)). According to the Lindemann melting criterion, melting occurs when $\overline{\Delta x}_m/l$ reaches a threshold value. If the difference of the displacements between the $\square$ and $\triangle$ lattices concentrate into a thin layer of liquid with a large $\overline{\Delta x}_m/l \gg 0.1$, the strong friction at the liquid-crystal interface would melt more crystal until $\overline{\Delta x}_m/l$ reaches the threshold of Lindemann melting criterion of 0.1. Thus, a larger shear displacement $\overline{\Delta x}_m$ will produce a liquid band with a thicker l, and $\overline{\Delta x}_m/l$ is a constant threshold value. Figure 2(d) further

shows that virtual melting is absent at $\gamma_m < 0.1$. We attribute this observation to fact that defect motions in the vicinity of the □–△ interface are sufficient to relax the system under weak applied shear stress.

□ and △ lattices exhibit different shear moduli G_{xz} in the shear plane (the xz plane), which can induce a nonzero $\overline{\Delta x}_m$. Since the interlayer separation of the □ crystal is smaller than that of the △ crystal, i.e. the height of a pyramid is smaller than a tetrahedron as shown in figure 2(c) inset. The longer interplanar spacing corresponds to a softer shear modulus, i.e. $G_{xz}^{\square} > G_{xz}^{\triangle}$. Larger $G_{xz}^{\square}$, in turn, is accompanied by smaller Δx, as observed in figure 2(b).

Strain energy dominates under large γ_m. Thus we measured the lattice strain during the □ → △ transition (figure 2 and supplementary figures S5 and S8). The local strain tensor, $\boldsymbol{\varepsilon}$, is determined by minimizing the mean square difference in the non-affine deformation $\sum_j (d_i - (\boldsymbol{\varepsilon}_i + \boldsymbol{I})D_{ij})^2$ [57, 58], where d_{ij} is the bond between particle i and its neighbor j, and D_{ij} is the reference bond of d_{ij} on a perfect lattice (supplementary information section 2.4 and supplementary figure S5(a)). For a quasi-2D sample, $\boldsymbol{\varepsilon}$ contains three independent components: the local shear strain, $\varepsilon_s = (\varepsilon_{12} + \varepsilon_{21})$, and the uniaxial strains, $\varepsilon_x = \varepsilon_{11}$, and $\varepsilon_y = \varepsilon_{22}$ along the x and y directions, respectively. These strains oscillate with the external shear (figures 2(e) and (f)), reflecting the fact that both lattices are periodically deformed. This behavior is quantitatively confirmed by the directly measured oscillating lattice constant (supplementary figures S3(b) and (c)). Since the driving shear is along the x direction, ε_x oscillates with a larger amplitude than ε_y in both lattices. The opposite phases between ε_x and ε_y arise from the positive Poisson's ratio of the colloidal crystals. Because the mean values $\bar{\varepsilon}_{x,y} \leqslant 0$ for the □ lattices in figure 2(e), the total volumetric strain $\bar{\varepsilon}_v = (\bar{\varepsilon}_x + \bar{\varepsilon}_y)/2 < 0$, i.e. the □ lattices are compressed. This phenomenon creates free volume to form liquid, facilitating virtual melting.

3.3. Shear-dependent nuclei orientations

The lattice orientation of the product phase strongly depends on the magnitude of the shear strain. For small $\gamma_m < 0.1$, the classic martensitic nucleation is featured with a fixed lattice misorientation angle $\theta = 15°$ (figure 3 blue box, supplementary figure S7(d)). It is due to formation of dislocation dipoles at the specific site of □ lattice (supplementary figures I(e)–(h)), and therefore, independent of the shear direction. Consequently, the orientation of nucleus lattice relative to the shear direction, α, is random in this region.

By contrast, under intermediate shear ($0.1 \leqslant \gamma_m < 0.4$), the coalescence of vacancies and dislocations produces liquid nuclei which then recrystallize into a △ lattice surrounded by a liquid ring. The liquid ring and △ lattice subsequently grow via diffusive nucleation. Such propagating solid–solid interface with an intermediate liquid has been suggested by simulations [6, 7]. The △ lattice orientation tends to align along the shear [32, 33], i.e. $\alpha \simeq 0$, to minimize interlayer friction (figure 3 red box), whilst θ is random. α and θ under different shear strains, summarized in figure 3, show that the lattice orientation of the nucleus is dominated by the ambient □ lattice under weak shear, and by the shear direction under strong shears. Thus, the intermediate shear can facilitate the formation of a single crystal [30, 32]. Increasing γ_m even further produces more liquid during the transition and eventually induces melting when $\gamma_m \geqslant 0.4$.

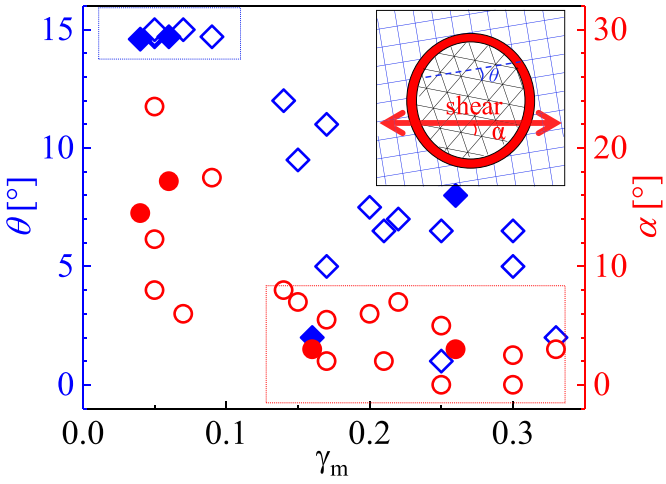

Figure 3. Lattice misorientation angle θ (diamonds) and shear misalignment angle α (circles) under different γ_m in 21 samples. $\theta \simeq 15°$ at small γ_m (blue box); $\alpha < 8°$ at large γ_m (red box); θ and α are random under other conditions. For a △-lattice nucleus in a □ lattice, the possible ranges are $0 \leqslant \theta \leqslant 15°$ and $0 \leqslant \alpha \leqslant 30°$. The empty and filled symbols are for □ → △ and 4□ → 3△ transitions, respectively. Only θ in the early-stage nucleation are shown. α is a constant over time.

4. Discussion

Peng *et al* [17, 18] about the similar colloidal systems focused on the initial critical nucleus formation stage without oscillatory shear because their later supercritical nucleus growth stage is normal: the growth front is a dry crystal–crystal interface in [17, 18] instead of a liquid band shown here. We focus on the later supercritical nucleus growth stage under shear and observe the following new results: (1) The growth front is a liquid band which experimentally confirms the theoretical prediction of virtual melting in [42] for the first time. (2) The liquid layer has a constant mean thickness l under a fixed shear strain amplitude γ_m (figure 1(i)); (3) l increases with γ_m (figure 2(d)); (4) The relative displacement per layer coincide with the Lindemann melting criterion, which provides an alternative explanation to virtual melting (figures 2(b)–(d)); (5) The lattice orientation of product phase is neither random as in [17], nor a special angle of 45° in [18], but depends on shear direction and the lattice orientation of the parent phase (figure 3). Additionally, the initial nucleation stage under shear exhibits an unclosed Burgers loop (figures 1(a)–(f)) which is different from that without shear in [17].

Many structural transitions in nature and industry are shear-induced, but their kinetics have not been experimentally observed at the single-particle level before. We directly visualize such process using a colloidal system and observed the virtual melting at the growth front. Shear-induced virtual melting at the crystalline interface has been predicted on the

basis of stress relaxation [4–9, 42, 59]. It has been mainly studied in simulations [4–11], and was confirmed indirectly in experiment at the $PbTiO_3$ surface [60] and Al–Fe interface [50]. In [50], the observed amorphous nano-layer at the interface was shown to be a liquid instead of an amorphous solid via simulation [50]. The lack of single-particle-level experimental observations has contributed to a limited understanding of the kinetic mechanisms underlying virtual melting. In our work, single-particle-level kinetics of virtual melting has been observed. The theory for virtual melting in [42] is not quantitatively tested because surface tension and strain energies are difficult to measure in colloidal crystals. Instead, our measurements provide an alternate explanation for the virtual melting on the basis of Lindemann melting criterion.

Different shear moduli of the two neighboring lattices could induce a shear displacement gradient across the interface. For samples under different shears, the ratio of the shear displacement across the interface to the liquid layer thickness is a constant with a value that is approximately the same as the Lindemann threshold for melting. This novel mechanism should similarly hold for grain boundaries in polycrystals and interfaces between two crystals in either 2D or 3D. For example, the shear-induced virtual melting is also observed at grain boundaries of a 35-layer polycrystals (movie S5). In addition, a transient liquid layer on a migrating grain boundary in strained aluminum polycrystals has been observed in a simulation [61]. Thus, virtual melting could generally arise and exist at interfaces under a sufficient shear, and could play an important role in shear-induced amorphization of covalent crystals [49, 62], metals and alloys [3]. Severe plastic deformations can also produce amorphous solids or amorphous-crystalline composites as super alloys [3]. However, little is known about their formation kinetics under strong shear, in large part because microscopic *in-situ* measurements in bulk are not available. Virtual melting induced by severe plastic deformation is difficult to observe because liquids rapidly crystallize or vitrify when the post-mortem sample is observed with the unloaded strain. The observed virtual melting suggests that plastic deformation may melt grain boundaries in polycrystals, which subsequently vitrify into amorphous regions after the stress is unloaded during fabrication of super alloys. In addition, the measured relations between two lattice orientations and the shear direction under different shear strains cast light on controlling lattice orientations in polycrystal fabrication.

Data availability statement

All data that support the findings of this study are included within the article (and any supplementary files).

Acknowledgments

We thank Qingping Sun, Xian Chen, Yang Xiang, Rui Zhang and Qi Zhang for helpful discussions. This work was supported by RGC GRF Grants 16302720 and 16305822; NSF Grant DMR20-03659, NSFC 12474206, and PENN MRSEC Grant DMR-2309043.

ORCID iDs

Wei Li https://orcid.org/0000-0003-0425-1723
Yilong Han https://orcid.org/0000-0002-1439-0121

References

[1] Porter D A and Easterling K E 2009 *Phase Transformations in Metals and Alloys (Revised Reprint)* (CRC press)
[2] Ross N L and Price G D 1992 The stability of minerals: an introduction *The Stability of Minerals* (Springer) pp 1–24
[3] Hua P, Xia M, Onuki Y and Sun Q 2021 Nanocomposite NiTi shape memory alloy with high strength and fatigue resistance *Nat. Nanotechnol.* **16** 409–13
[4] Levitas V I and Ravelo R 2012 Virtual melting as a new mechanism of stress relaxation under high strain rate loading *Proc. Natl Acad. Sci. USA* **109** 13204–7
[5] Levitas V I and Momeni K 2014 Solid–solid transformations via nanoscale intermediate interfacial phase: multiple structures, scale and mechanics effects *Acta Mater.* **65** 125–32
[6] Momeni K and Levitas V I 2014 Propagating phase interface with intermediate interfacial phase: phase field approach *Phys. Rev.* B **89** 184102
[7] Momeni K, Levitas V I and Warren J A 2015 The strong influence of internal stresses on the nucleation of a nanosized, deeply undercooled melt at a solid–solid phase interface *Nano Lett.* **15** 2298–303
[8] Momeni K and Levitas V I 2015 A phase-field approach to solid–solid phase transformations via intermediate interfacial phases under stress tensor *Int. J. Solids Struct.* **71** 39–56
[9] Momeni K and Levitas V I 2016 A phase-field approach to nonequilibrium phase transformations in elastic solids via an intermediate phase (melt) allowing for interface stresses *Phys. Chem. Chem. Phys.* **18** 12183–203
[10] Wen L, Wu H, Sun H and Chen C 2019 Profound softening and shear-induced melting of diamond under extreme conditions: an ab-initio molecular dynamics study *Carbon* **155** 361–8
[11] Zarkevich N A, Chen H, Levitas V I and Johnson D D 2018 Lattice instability during solid-solid structural transformations under a general applied stress tensor: example of Si I → Si II with metallization *Phys. Rev. Lett.* **121** 165701
[12] Li B, Zhou Di and Han Y 2016 Assembly and phase transitions of colloidal crystals *Nat. Rev. Mater.* **1** 15011
[13] Anderson V J and Lekkerkerker H N W 2002 Insights into phase transition kinetics from colloid science *Nature* **416** 811–5
[14] Frenkel D 2002 Playing tricks with designer "atoms" *Science* **296** 65–66
[15] Crocker J C and Grier D G 1996 Methods of digital video microscopy for colloidal studies *J. Colloid Interface Sci.* **179** 298–310
[16] Pusey P N and Van Megen W 1986 Phase behaviour of concentrated suspensions of nearly hard colloidal spheres *Nature* **320** 340–2
[17] Peng Y, Wang F, Wang Z, Alsayed A M, Zhang Z, Yodh A G and Han Y 2015 Two-step nucleation mechanism in solid–solid phase transitions *Nat. Mater.* **14** 101–8
[18] Peng Y, Li W, Wang F, Still T, Yodh A G and Han Y 2017 Diffusive and martensitic nucleation kinetics in solid–solid transitions of colloidal crystals *Nat. Commun.* **8** 14978
[19] Casey M T, Scarlett R T, Benjamin Rogers W, Jenkins I, Sinno T and Crocker J C 2012 Driving diffusionless transformations in colloidal crystals using dna handshaking *Nat. Commun.* **3** 1209

[20] Jenkins I C, Casey M T, McGinley J T, Crocker J C and Sinno T 2014 Hydrodynamics selects the pathway for displacive transformations in dna-linked colloidal crystallites *Proc. Natl Acad. Sci. USA* **111** 4803–8

[21] Fang H, Hagan M F and Benjamin Rogers W 2020 Two-step crystallization and solid–solid transitions in binary colloidal mixtures *Proc. Natl Acad. Sci. USA* **117** 27927–33

[22] Immink J N, Bergman M J, Erik Maris J J, Stenhammar J and Schurtenberger P 2020 Crystal-to-crystal transitions in binary mixtures of soft colloids *ACS Nano* **14** 14861–8

[23] Yang Y, Fu L, Marcoux C, Socolar J E S, Charbonneau P and Yellen B B 2015 Phase transformations in binary colloidal monolayers *Soft Matter* **11** 2404–15

[24] Du C X, van Anders G, Newman R S and Glotzer S C 2017 Shape-driven solid–solid transitions in colloids *Proc. Natl Acad. Sci. USA* **114** E3892–9

[25] Li M, Yue Z, Chen Y, Tong H, Tanaka H and Tan P 2021 Revealing thermally-activated nucleation pathways of diffusionless solid-to-solid transition *Nat. Commun.* **12** 4042

[26] Yethiraj A, Wouterse A, Groh B and van Blaaderen A 2004 Nature of an electric-field-induced colloidal martensitic transition *Phys. Rev. Lett.* **92** 058301

[27] Mohanty P S, Bagheri P, Nöjd S, Yethiraj A and Schurtenberger P 2015 Multiple path-dependent routes for phase-transition kinetics in thermoresponsive and field-responsive ultrasoft colloids *Phys. Rev.* X **5** 011030

[28] Amos R M, Rarity J G, Tapster P R, Shepherd T J and Kitson S C 2000 Fabrication of large-area face-centered-cubic hard-sphere colloidal crystals by shear alignment *Phys. Rev.* E **61** 2929

[29] Besseling T H, Hermes M, Fortini A, Dijkstra M, Imhof A and Van Blaaderen A 2012 Oscillatory shear-induced 3D crystalline order in colloidal hard-sphere fluids *Soft Matter* **8** 6931–9

[30] Vickreva O, Kalinina O and Kumacheva E 2000 Colloid crystal growth under oscillatory shear *Adv. Mater.* **12** 110–2

[31] Lavergne F A, Curran A, Aarts D G A L and Dullens R P A 2018 Dislocation-controlled formation and kinetics of grain boundary loops in two-dimensional crystals *Proc. Natl Acad. Sci. USA* **115** 6922–7

[32] Li W, Peng Y, Zhang Y, Still T, Yodh A G and Han Y 2020 Shear-assisted grain coarsening in colloidal polycrystals *Proc. Natl Acad. Sci. USA* **117** 24055–60

[33] Wu M W, Register R A and Chaikin P M 2006 Shear alignment of sphere-morphology block copolymer thin films with viscous fluid flow *Phys. Rev.* E **74** 040801

[34] Solomon T and Solomon M J 2006 Stacking fault structure in shear-induced colloidal crystallization *J. Chem. Phys.* **124** 134905

[35] Gokhale S, Nagamanasa K H, Santhosh V, Sood A K and Ganapathy R 2012 Directional grain growth from anisotropic kinetic roughening of grain boundaries in sheared colloidal crystals *Proc. Natl Acad. Sci. USA* **109** 20314–9

[36] Cohen I, Mason T G and Weitz D A 2004 Shear-induced configurations of confined colloidal suspensions *Phys. Rev. Lett.* **93** 046001

[37] Cohen I, Davidovitch B, Schofield A B, Brenner M P and Weitz D A 2006 Slip, yield and bands in colloidal crystals under oscillatory shear *Phys. Rev. Lett.* **97** 215502

[38] Wu Y L, Derks D, van Blaaderen A and Imhof A 2009 Melting and crystallization of colloidal hard-sphere suspensions under shear *Proc. Natl Acad. Sci. USA* **106** 10564–9

[39] Derks D, Wu Y L, van Blaaderen A and Imhof A 2009 Dynamics of colloidal crystals in shear flow *Soft Matter* **5** 1060–5

[40] López-Barrón C R, Porcar L, Eberle A P R and Wagner N J 2012 Dynamics of melting and recrystallization in a polymeric micellar crystal subjected to large amplitude oscillatory shear flow *Phys. Rev. Lett.* **108** 258301

[41] Ruiz-Franco J, Marakis J, Gnan N, Kohlbrecher J, Gauthier M, Lettinga M P, Vlassopoulos D and Zaccarelli E 2018 Crystal-to-crystal transition of ultrasoft colloids under shear *Phys. Rev. Lett.* **120** 078003

[42] Levitas V I, Henson B F, Smilowitz L B and Asay B W 2004 Solid–solid phase transformation via virtual melting significantly below the melting temperature *Phys. Rev. Lett.* **92** 235702

[43] Alsayed A M, Islam M F, Zhang J, Collings P J and Yodh A G 2005 Premelting at defects within bulk colloidal crystals *Science* **309** 1207–10

[44] Wang Z, Wang F, Peng Y, Zheng Z and Han Y 2012 Imaging the homogeneous nucleation during the melting of superheated colloidal crystals *Science* **338** 87–90

[45] Schmidt M and Löwen H 1997 Phase diagram of hard spheres confined between two parallel plates *Phys. Rev.* E **55** 7228

[46] Fortini A and Dijkstra M 2006 Phase behaviour of hard spheres confined between parallel hard plates: manipulation of colloidal crystal structures by confinement *J. Condens. Matter Phys.* **18** L371

[47] Oğuz E C, Marechal M, Ramiro-Manzano F, Rodriguez I, Messina R, Meseguer F J and Löwen H 2012 Packing confined hard spheres denser with adaptive prism phases *Phys. Rev. Lett.* **109** 218301

[48] Pieranski P, Strzelecki L and Pansu B 1983 Thin colloidal crystals *Phys. Rev. Lett.* **50** 900

[49] He Y, Zhong Li, Fan F, Wang C, Zhu T and Mao S X 2016 In situ observation of shear-driven amorphization in silicon crystals *Nat. Nanotechnol.* **11** 866–71

[50] Liu F C, Dong P, Zhang J, Lu W, Taub A and Sun K 2020 Alloy amorphization through nanoscale shear localization at Al–Fe interface *Mater. Today Phys.* **15** 100252

[51] Dash J G, Rempel A W and Wettlaufer J S 2006 The physics of premelted ice and its geophysical consequences *Rev. Mod. Phys.* **78** 695

[52] Woodruff D P 1973 *The Solid-Liquid Interface* (CUP Archive)

[53] Mei Q S and Lu K 2007 Melting and superheating of crystalline solids: from bulk to nanocrystals *Prog. Mater. Sci.* **52** 1175–262

[54] Wang F, Zhou Di and Han Y 2016 Melting of colloidal crystals *Adv. Funct. Mater.* **26** 8903–19

[55] Jin Z H, Gumbsch P, Lu K and Ma E 2001 Melting mechanisms at the limit of superheating *Phys. Rev. Lett.* **87** 055703

[56] Hoffmann G P and Löwen H 2001 Freezing and melting criteria in non-equilibrium *J. Phys.: Condens. Matter* **13** 9197

[57] Falk M L and Langer J S 1998 Dynamics of viscoplastic deformation in amorphous solids *Phys. Rev.* E **57** 7192

[58] Schall P, Cohen I, Weitz D A and Spaepen F 2006 Visualizing dislocation nucleation by indenting colloidal crystals *Nature* **440** 319–23

[59] Levitas V I 2005 Crystal-amorphous and crystal-crystal phase transformations via virtual melting *Phys. Rev. Lett.* **95** 075701

[60] Levitas V I, Ren Z, Zeng Y, Zhang Z and Han G 2012 Crystal-crystal phase transformation via surface-induced virtual premelting *Phys. Rev.* B **85** 220104

[61] Umar Dad M, Perveen A, Liang H and Yang Y 2021 Interface migration in aluminum bicrystals via premelting *Surf. Interface* **26** 101344

[62] Zhao S, Hahn E N, Kad B, Remington B A, Wehrenberg C E, Bringa E M and Meyers M A 2016 Amorphization and nanocrystallization of silicon under shock compression *Acta Mater.* **103** 519–33